Electro-Thermal Management and Degradation Forecasting of Power Electronics Building Blocks in All-Electric Ships

Ali Moghassemi*, Laxman Timilsina*, S M Imrat Rahman*, Ali Arsalan†, Elutunji Buraimoh*, Gokhan Ozkan*,‡, Behnaz Papari*,†, Christopher S. Edrington*, Zheyu Zhang§
Emails: {amoghas;ltimils;smimrar;aarsala;eburaim;gokhano;bpapari;cedring}@clemson.edu, zhangz49@rpi.edu
*Holcombe Department of Electrical and Computer Engineering, Clemson University, Clemson 29634, SC, USA
†Department of Automotive Engineering, Clemson University, Greenville 29607, SC, USA
‡Dominion Energy Innovation Center, Clemson University, North Charleston 29405, SC, USA
§Electrical, Computer, and Systems Engineering, Rensselaer Polytechnic Institute, Troy 12180, NY, USA

2025 IEEE Electric Ship Technologies Symposium (ESTS) | 979-8-3315-2517-0/25/$31.00 ©2025 IEEE | DOI: 10.1109/ESTS62818.2025.11152422

***Abstract*—The Power Electronics Building Block (PEBB) concept integrates fundamental components into modular units, scalable for All-Electric Ships (AESs) through Modular Multi-level Converters (MMCs). MMC-based PEBBs offer modularity, low switching losses, good voltage and current quantization, and high efficiency. However, switching frequency greatly impacts converter design, influencing size, cost, and component stress. Higher frequencies reduce reactive component size but increase thermal stress and degradation of power modules. This paper proposes a Finite-Control Set Model Predictive Control (FCS-MPC) method for multi-objective electro-thermal management of PEBBs, integrating a Deep Neural Network (DNN)-based degradation forecasting model. Results demonstrate the method's ability to maintain power quality, regulate junction temperature, and provide accurate degradation forecasts, enhancing reliability and mitigating aging.**

***Index Terms*—PEBB, Electro-Thermal Management, FCS-MPC, Degradation Forecasting, DNN.**

I. Introduction

The increasing demand for power in modern naval ships has led to the development of All-Electric Ships (AESs), which rely on electrical energy for propulsion, weapons, and onboard services. These ships use power electronic interfaces to connect loads to their energy sources, driving interest in multi-functional power converters for better energy conversion and management [1]. New technologies, such as wide bandgap materials, silicon carbide semiconductors, and Power Electronics Building Blocks (PEBB), are transforming marine systems, moving away from traditional steamships and sailing vessels. The PEBB concept, introduced by the US Office of Naval Research (ONR) in 1998, aimed to improve converter availability, performance, and cost-effectiveness in AESs [2].

Quality-of-Service (QoS) metric plays a key role in planning and operating AESs [3]. QoS measures the system's ability to provide continuous power to mission-critical loads. Several factors influence QoS, including the ratings and reliability of prime movers, power conversion equipment, load requirements, and system design. Power converters should incorporate features such as hot-swappable modules and built-in redundancy to ensure smooth operation and reduce downtime, following the Least Replacement Unit (LRU) principle. AESs require compact and reliable converters to maximize available space and enhance operational reliability. A major challenge in power converter design is ensuring high power quality while dealing with thermal and mechanical constraints. From a control perspective, key challenges include power quality, thermal stress, and voltage stress on semiconductors [4], [5].

One critical aspect of switched power converter design is the choice of switching frequency. Semiconductors operate as switches, rapidly transitioning between states. Increasing the switching frequency allows for smaller reactive components, reducing the converter's size, weight, and cost. However, the frequency is often limited by the device's capabilities, which must balance factors like voltage, current, conduction, and switching losses [6]. Other components, such as capacitors and inductors, can be optimized to minimize losses at a given switching frequency while maintaining acceptable voltage and current ripples. However, high switching frequencies, combined with varying operating conditions, lead to thermal stress on semiconductor devices. Repeated heating and cooling cycles can cause aging or failure, increasing maintenance costs and reducing system availability [7].

To ensure reliability without oversizing components, designs often target specific reliability goals by controlling factors such as maximum junction temperature and current ratings [8]. Active thermal management is used to regulate junction temperatures, helping manage thermal stress and improve efficiency. Active thermal management can be implemented through various methods, such as adjusting cooling system speed or controlling electrical parameters [9]. Switching frequency adjustments can help manage thermal stress by reducing switching losses when loads increase. Studies have shown that adaptive frequency control based on load conditions can effectively limit thermal cycling [7]. Simple control methods,

This material is based upon research supported by the US Office of Naval Research (ONR) under award number N00014-22-1-2558, and it is approved for public release under DCN# 2025-1-23-540.

such as feedback loops, can help optimize switching frequency to balance performance and power quality [10].

A. Contribution and Structure of the Paper

This paper proposes a Finite-Control Set Model Predictive Control (FCS-MPC) strategy to regulate the electrical and thermal performances of PEBBs. FCS-MPC offers fast response times and flexible control, allowing multiple objectives to be handled within a single framework. The proposed approach is applied to a five-level Modular Multi-level Converter (MMC) connected to an Induction Machine (IM), with the control performance evaluated through simulations. Further, a Deep Neural Network (DNN) based degradation model is proposed to predict power loss in PEBBs under different conditions. By defining failure thresholds and incorporating degradation data, the model helps optimize the electro-thermal management strategy within the FCS-MPC framework.

The paper is organized as follows. Section II presents the concept and mathematical model of the MMC-based PEBB system. Section III details the proposed FCS-MPC electro-thermal management approach, including power loss and thermal models. Section IV discusses simulation results based on different weight factors. Plus, this section introduces the DNN-based degradation model and its integration into the control strategy. Finally, Section V concludes the paper.

II. Power Electronics Building Block (PEBB)

A. Principle and Mathematical Model

The PEBB concept can effectively be realized by the MMC topology, where each Submodule (SM) functions as a PEBB block. Figure 1 illustrates the MMC-based PEBB configuration. This topology consists of three legs corresponding to the three phases, with each leg comprising two arms: the upper and the lower arms. Each arm includes n identical SMs connected in series. These SMs can be configured as full-bridge, half-bridge, or a combination. This study adopts the widely utilized half-bridge SM configuration, which comprises two complementary MOSFETs with anti-parallel diodes and a parallel capacitor. Each leg contains an arm inductor, L_{arm}, which limits short-circuit currents. A series resistor, R_{arm}, may also be included to reduce power losses in the MMC.

This paper presents the equations for phase a, and similar formulations can be applied to other phases. As depicted in Figure 1, the SM output terminals are connected in series to form the arm voltage. Here, V_{a1}^U, V_{a2}^U, ..., V_{an}^U represent the output voltages of individual SMs. The following notation is adopted: Subscripts a, b, and c denote phases; U and L denote upper and lower arms; n is the number of SMs; L_{arm} and R_{arm} are the arm inductance and resistance, respectively; V_a^U, V_b^U, V_c^U are upper arm voltages, and V_a^L, V_b^L, V_c^L are lower arm voltages; i_a^U, i_b^U, i_c^U are upper arm currents, and i_a^L, i_b^L, i_c^L are lower arm currents; i_{OA}, i_{OB}, i_{OC} are the output currents; i_{circ}^a, i_{circ}^b, i_{circ}^c are circulating currents; V_{dc} is the DC source voltage; $V_C^{aU,1}$ to $V_C^{cL,n}$ are the SM capacitor voltages. Each SM is connected or bypassed based on its MOSFET states. The upper and lower MOSFETs operate complementarily: when

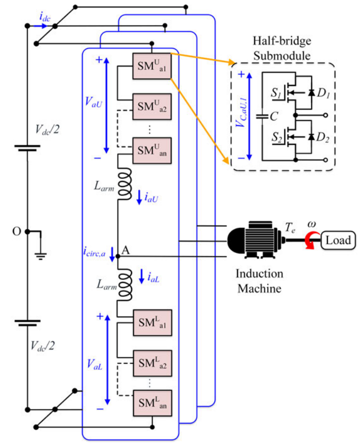

Fig. 1. MMC-based PEBB concept

one is ON, the other is OFF. Ref. [11] provided the details of switching states.

Applying Kirchhoff's Current Law (KCL) to the circuit in Figure 1, the output current is given by:

$$i_{OA} = i_a^U - i_a^L \tag{1}$$

The circulating current is the average of the arm currents:

$$i_{circ}^a = \frac{i_a^U + i_a^L}{2} \tag{2}$$

Using Kirchhoff's Voltage Law (KVL), the arm voltage equations are expressed as:

$$\frac{V_{dc}}{2} - V_a^U - L_{arm}\frac{di_a^U}{dt} - R_L i_{OA} - L_L\frac{di_{OA}}{dt} = 0 \tag{3}$$

$$-\frac{V_{dc}}{2} + V_a^L + L_{arm}\frac{di_a^L}{dt} - R_L i_{OA} - L_L\frac{di_{OA}}{dt} = 0 \tag{4}$$

By substituting i_{OA} from (1) into the sum of (3) and (4), the output voltage, V_{OA}, is:

$$V_{OA} = R_L i_{OA} + L_L\frac{di_{OA}}{dt} = \frac{V_a^L - V_a^U}{2} - L_{arm}\frac{di_{OA}}{dt} \tag{5}$$

The arm voltages can be represented as:

$$V_a^U = n_{SM}^U \cdot \overline{V_C^{aU}} \tag{6}$$

$$V_a^L = n_{SM}^L \cdot \overline{V_C^{aL}} \tag{7}$$

Where n_{SM}^U and n_{SM}^L denote the number of connected SMs in the upper and lower arms, respectively, while $\overline{V_C^{aU}}$ and $\overline{V_C^{aL}}$ are the average SM capacitor voltages. Assuming the capacitor voltages remain constant at their nominal values $V_C^* = \frac{V_{dc}}{n-1}$, and neglecting the voltage drop across the arm inductors, the output voltage simplifies to:

$$V_{OA} = \left(\frac{n_{SM}^L - n_{SM}^U}{2}\right) \cdot V_C^* \tag{8}$$

III. Electro-Thermal Management with Finite-Control Set Model Predictive Control (FCS-MPC)

A. Model Predictive Control (MPC)

Linear control methods are commonly used in power converters but have limitations in handling complex applications. Sequence-Based Control (SBC) offers a more robust alternative that is widely applied in different applications such as motor drives and renewable energy systems. SBC leverages a mathematical model to predict system variables over a defined horizon, optimizing performance metrics like Total Harmonic Distortion (THD) and thermal regulation through a cost function that incorporates multiple constraints [12]. Model Predictive Control (MPC), a popular SBC method, uses system dynamics to predict future outputs and optimize control actions. MPC is categorized into the finite control set (FCS-MPC), which applies direct control signals, leading to variable switching frequencies and the infinite control set (ICS-MPC), which relies on modulation for fixed switching frequencies.

The SBC design process involves modeling the power converter, defining control variable relationships, and constructing a cost function to optimize efficiency, reliability, and performance. By incorporating multiple weighted constraints, SBC achieves superior electro-thermal management and system performance compared to traditional linear control techniques.

1) Mathematical Model: Switching devices such as MOSFETs operate as ideal switches with two distinct states: ON and OFF. The total number of possible switching states (PSS) can be determined by $PSS = x^l$, in which x represents the number of possible states per leg, and l denotes the number of legs. Power converter topologies vary based on application requirements. For example, the total number of switching states in a neutral-point-clamped (NPC) converter is $PSS = 3^3 = 27$. As the number of phases and levels in the converter increases, the PSS grows exponentially, imposing significant computational demands on the controller. This necessitates substantial processing power, which can be inefficient. To simplify computations, some switching states can be omitted. For instance, a two-level three-phase converter has eight switching states, yet these yield only seven distinct voltage vectors. Therefore, states producing the same voltage vector can be merged to optimize computational efficiency.

The Clarke transformation can be applied to voltage and current signals to streamline the system further and reduce computational costs. The Clarke transform for three-phase currents is expressed as follows:

$$i_{\alpha\beta 0}(t) = \frac{2}{3}\begin{bmatrix} 1 & -\frac{1}{2} & -\frac{1}{2} \\ 0 & \frac{\sqrt{3}}{2} & -\frac{\sqrt{3}}{2} \\ \frac{1}{2} & \frac{1}{2} & \frac{1}{2} \end{bmatrix}\begin{bmatrix} i_a(t) \\ i_b(t) \\ i_c(t) \end{bmatrix} \tag{9}$$

Similarly, the stationary $\alpha\beta$ frame transformation can be applied to voltage signals, defining current and voltage vectors as follows (omitting the time dependency for simplicity):

$$i = \begin{bmatrix} i_\alpha & i_\beta & i_0 \end{bmatrix}, v = \begin{bmatrix} v_\alpha & v_\beta & v_0 \end{bmatrix} \tag{10}$$

Thus, the equations in the stationary $\alpha\beta$ frame can be expressed as:

$$\frac{V_{dc}}{2} - V_a^U(t) - L_{arm}\frac{di(t)}{dt} - R_L i(t) - L_L\frac{di(t)}{dt} = 0 \tag{11}$$

$$-\frac{V_{dc}}{2} + V_a^L(t) + L_{arm}\frac{di(t)}{dt} - R_L i(t) - L_L\frac{di(t)}{dt} = 0 \tag{12}$$

The continuous-time nature of these equations poses challenges for implementation in digital controllers. Therefore, discretization techniques such as forward Euler, backward Euler, and Runge-Kutta approximations are used to convert continuous-time expressions into discrete-time forms. Each method introduces varying levels of accuracy and computational complexity. In this study, the forward Euler method is selected for its simplicity and acceptable precision. The forward Euler approximation is defined as:

$$\frac{dx}{dt} \approx \frac{x(k+1) - x(k)}{T_s} \tag{13}$$

The discretized forms of equations (11) and (12) with a single prediction horizon are:

$$\begin{aligned} \frac{V_{dc}}{2} - V_a^U(k) - L_{arm}\frac{i(k+1) - i(k)}{T_s} \\ -R_L i(k) - L_L\frac{i(k+1) - i(k)}{T_s} = 0 \end{aligned} \tag{14}$$

$$\begin{aligned} -\frac{V_{dc}}{2} + V_a^L(k) + L_{arm}\frac{i(k+1) - i(k)}{T_s} \\ -R_L i(k) - L_L\frac{i(k+1) - i(k)}{T_s} = 0 \end{aligned} \tag{15}$$

Where T_s is the sampling period. The predicted current can be expressed as:

$$i(k+1) = \left(\frac{T_s}{L_{arm} + L}\right)\left(\frac{V_{dc}}{2} - V_a^U(k) - Ri(k)\right) + i(k) \tag{16}$$

$$i(k+1) = \left(\frac{T_s}{L_{arm} - L}\right)\left(\frac{V_{dc}}{2} - V_a^L(k) + Ri(k)\right) + i(k) \tag{17}$$

For a five-level MMC-based PEBB and considering all switching states, there are a total of 125 voltage vectors ($PSS = 5^3 = 125$), as illustrated in Figure 2, but only 61 distinct voltage vectors are calculated. Adding additional levels to the MMC-based PEBB structure introduces new hexagonal rings of equilateral triangles, expanding the voltage space.

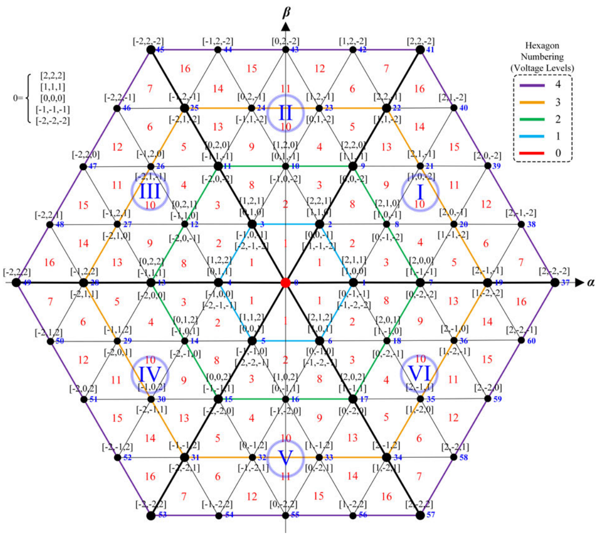

Fig. 2. Voltage vectors and switching states for a five-level MMC-based PEBB concept

B. Power Loss Model

Active thermal management leverages temperature-based control strategies, such as switching sequences, to regulate device temperatures. The primary goals are minimizing switching module losses, reducing thermal stress, and improving efficiency. This approach slows semiconductor degradation, lowers energy costs, and enhances system reliability. Higher switching frequencies reduce the size and weight of power converters, which is critical for applications with space and weight constraints, like ship power systems. However, this increases heat dissipation in semiconductor modules, necessitating effective cooling systems. The maximum junction temperature determines the required thermal resistance and, consequently, the heat sink size, impacting system cost and power density. Minimizing junction temperature through optimized control strategies and material selection can reduce heat sink size and cost.

The dominant power losses in converters are switching and conduction losses. Power losses are calculated based on predicted currents and device characteristics, typically obtained from manufacturer datasheets. The ON-state current of MOSFETs and diodes is derived from phase current and switching states.

Switching losses, categorized into turn-on and turn-off events, are modeled using reference energies provided by manufacturers. For varying operating conditions, switching energy dissipation is estimated as follows:

$$E_{sw} = E_{sw,ref}\left(\frac{i}{i_{ref}}\right)^{K_i}\left(\frac{v_{cc}}{v_{cc,ref}}\right)^{K_v} \cdot \left(1 + TC_{sw}\left(T_j - T_{j,ref}\right)\right) \tag{18}$$

Where i, v_{cc}, and T_j are operating conditions, while i_{ref}, $v_{cc,ref}$, $T_{j,ref}$, and $E_{sw,ref}$ are reference conditions. K_i, K_v, and TC_{sw} account for current, voltage, and temperature dependencies, respectively.

Conduction losses for MOSFETs and diodes are as follows:

$$P_{c,mosfet} = v_{CE,sat} \cdot i_C \tag{19}$$

$$P_{c,diode} = v_f \cdot i_f \tag{20}$$

Thus, total losses are calculated as:

$$P_{sw,loss} = \frac{E_{sw,mosfet} + E_{sw,diode}}{T_s} \tag{21}$$

$$P_{c,loss} = P_{c,mosfet} + P_{c,diode} \tag{22}$$

$$P_{t,loss} = P_{sw,loss} + P_{c,loss} \tag{23}$$

These equations accurately estimate power losses, enabling effective thermal management and optimization of control systems.

C. Thermal Model

The thermal performance of switching modules significantly impacts power converters' reliability, efficiency, and cost. Junction temperature estimation is crucial for thermal management, but real-time simulation is challenging due to the complex 3D nature of heat transfer [13]. Finite Element Analysis (FEA) provides detailed thermal modeling. Still, it is computationally intensive and often impractical for real-time applications due to high complexity and the lack of detailed material information from manufacturers [8]. Simplified thermal models focusing on dominant heat transfer paths are commonly used to address this. In most cases, heat flows primarily from the chip to the base plate, with secondary paths involving surface conduction and chip cross-coupling. A single heat transfer path model is sufficient for practical applications and aligns with manufacturer datasheets [9].

Thermal impedance is typically represented using thermal resistors and capacitors, where resistance reflects heat dissipation and capacitance accounts for energy storage. Although resistance may change over a semiconductor's lifetime due to aging, these changes are generally slow. The key inputs for thermal models are ambient temperature and power losses, which influence thermal cycling. Commonly used models include Cauer and Foster networks, which approximate the thermal response using lumped parameters [8]. This paper adopts the Cauer thermal network, widely used to model semiconductors.

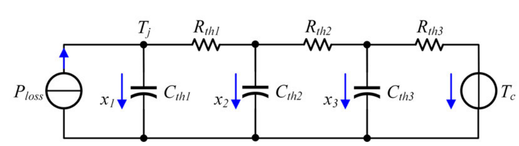

Fig. 3. Third-order Cauer thermal network

A third-order Cauer network, shown in Figure 3, models each layer of the semiconductor module with thermal resistances R_{th} and capacitances C_{th}. Using Kirchhoff's Current Law (KCL), the thermal network's state equations are:

$$\frac{dx_1}{dt} = -\frac{1}{C_{th1}R_{th1}}x_1 + \frac{1}{C_{th1}R_{th1}}x_2 + \frac{1}{C_{th1}}P_{t,loss}(t) \quad (24)$$

$$\frac{dx_2}{dt} = \frac{1}{C_{th2}R_{th1}}x_1 - \frac{(R_{th1}+R_{th2})}{C_{th2}R_{th1}R_{th2}}x_2 + \frac{1}{C_{th2}R_{th2}}x_3 \quad (25)$$

$$\frac{dx_3}{dt} = \frac{1}{C_{th3}R_{th2}}x_2 - \frac{(R_{th2}+R_{th3})}{C_{th3}R_{th2}R_{th3}}x_3 + \frac{1}{C_{th3}}T_c(t) \quad (26)$$

Where x_1, x_2, and x_3 are the temperatures of the thermal capacitors, $P_{total,loss}(t)$ represents power loss, and $T_c(t)$ is the base plate temperature. The Cauer network provides a balance between accuracy and computational efficiency, making it suitable for real-time applications.

D. Cost Function

Effectively controlling system parameters requires balancing multiple objectives rather than focusing on a single goal. To achieve this, static and dynamic constraints are defined for each objective, forming the basis for a multi-objective optimization framework. The key control objectives in this study are electrical regulation, which ensures stable operation of the converter by maintaining the input voltage and output voltages and currents within desired limits, and thermal management, which actively regulates the junction temperature and power loss regulation of PEBBs. The cost function for stabilizing the electrical objective is discussed first, followed by a thermal objective term, which accounts for losses and junction temperature regulation of the semiconductor devices.

For electrical performance, the cost function evaluates the error between predicted and reference current values:

$$OF_E = |i_\alpha^*(k+1) - i_\alpha(k+1)| + \left|i_\beta^*(k+1) - i_\beta(k+1)\right| \quad (27)$$

Here, $i_\alpha^*(k+1)$ and $i_\beta^*(k+1)$ are the reference current signals for the next time step, while $i_\alpha(k+1)$ and $i_\beta(k+1)$ are the predicted currents for a given voltage vector. In high-frequency switching, the present current vector can approximate the reference values due to minimal change. However, this assumption may lead to delays and reduced stability in low-frequency switching.

For thermal performance, an additional cost function minimizes the deviation between the predicted junction temperature and its reference value [11]:

$$OF_T = \left|T_j^*(k+1) - T_j(k+1)\right| \quad (28)$$

Where $T_j^*(k+1)$ and $T_j(k+1)$ represent the reference and predicted junction temperature values, respectively. To integrate electrical and thermal objectives, a multi-objective cost function is defined using (27) and (28) with weighting factors:

$$OF_{ET} = \omega_E OF_E + \omega_T OF_T \quad (29)$$

Where ω_E and ω_T, as the electrical and thermal weight factors, are normalized to ensure balance:

$$\omega_E + \omega_T = 1 \quad (30)$$

By tuning ω_E and ω_T, the control system can prioritize either electrical performance or thermal management. Minimizing the weighted cost function allows for dynamic trade-offs, effectively balancing electrical and thermal performance while ensuring robust and reliable converter operation.

IV. Simulation Results

This section demonstrates the implementation and evaluation of the proposed FCS-MPC strategy for the electro-thermal management of the PEBBs. Figure 4 presents the control block diagram for the FCS-MPC-based electro-thermal management approach. The control strategy integrates both electrical and thermal models to optimize the performance of a five-level PEBB connected to an IM. Each SM within the PEBB is equipped with individual thermal and power loss models, enabling detailed electro-thermal analysis and control.

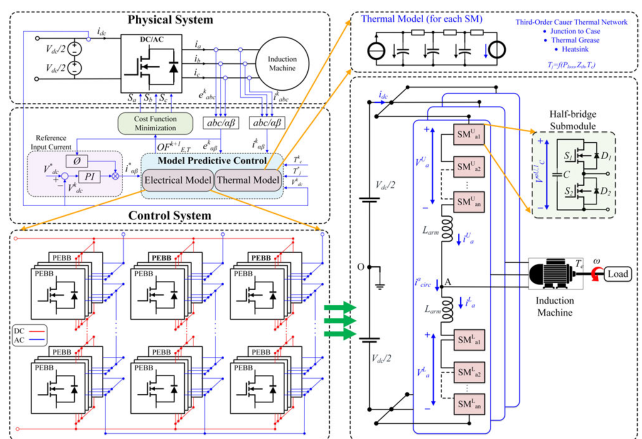

Fig. 4. Control block diagram of the proposed FCS-MPC-based electro-thermal management system

The simulation validates the performance of the FCS-MPC for a five-level PEBB system comprising four SMs per arm, totaling 24 SMs across the entire converter. Each SM is configured as a half-bridge converter with two complementary MOSFETs, anti-parallel diodes, and a parallel capacitor. The system parameters are detailed in Table I.

A. Performance Evaluation

The tuning of weighting factors ω_T and ω_E is critical for balancing thermal and electrical performance. The tuning process, conducted under low power operation for accuracy, evaluated electrical weight factors ω_E in increments of 0.1

TABLE I
SIMULATION PARAMETERS

Parameters	Value	Unit
PEBB		
DC-link voltage, V_{dc}	500	V
Number of SMs per arm, n	4	-
SM capacitance, C_m	105	mF
Arm inductance, L_{arm}	5	mH
Arm resistance, R_{arm}	0.25	Ω
Switching frequency, F_{sw}	10	kHz
Simulation sampling time, T_s	20	μs
Control sampling time	12	μs
IM		
Stator phase resistance, R_s	0.5968	Ω
Rotor phase resistance (referred to stator), R_r'	0.6258	Ω
Stator leakage inductance, L_{ls}	0.005473	H
Rotor leakage inductance (referred to stator), L_{lr}'	0.005473	H
Magnetizing inductance, L_m	0.0354	H
Number of pole pairs	2	-
Combined rotor and load moment of inertia, J_m	0.05	kg·m^2
Viscous friction coefficient, b	0.005879	Nms
Proportional gain, K_p	5	-
Integral gain, K_i	50	-

from 0.1 to 0.9. The tuning ensures optimal integration of the electrical and thermal characteristics of the system within the multi-objective cost function.

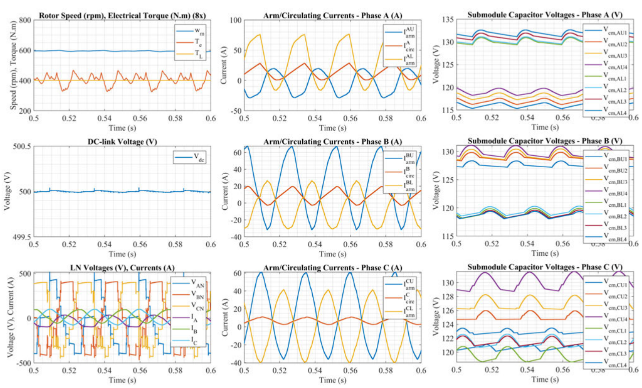

(a) Electrical performance

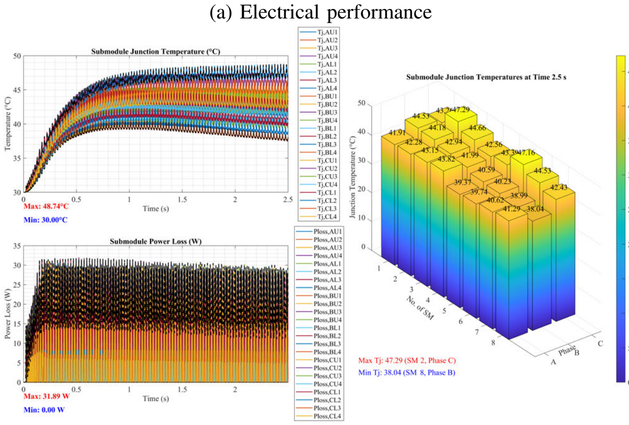

(b) Thermal performance

Fig. 5. PEBB's electrical and thermal performances with $\omega_E = 0.1$

1) *Electrical Performance:* Simulations analyzed the effect of varying ω_E on the performance. Figures 5a and 6a illustrate

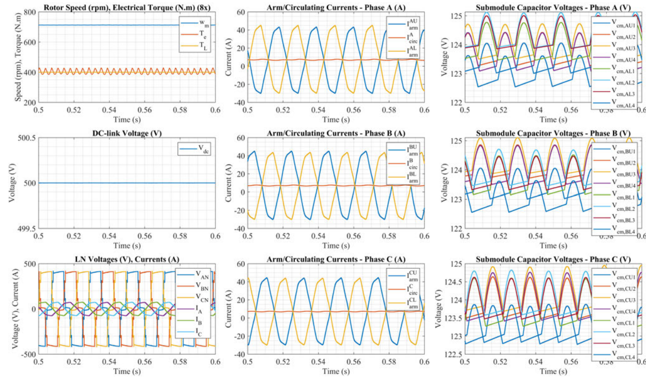

(a) Electrical performance

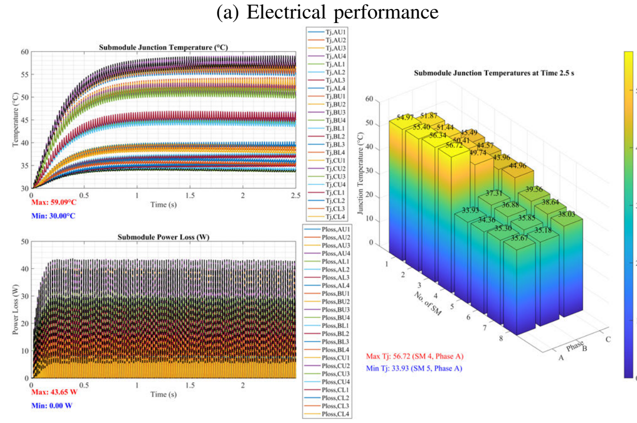

(b) Thermal performance

Fig. 6. PEBB's electrical and thermal performances with $\omega_E = 0.9$

the electrical performance for ω_E values of 0.1 and 0.9, respectively. For lower ω_E values, the current THD, DC-link voltage ripple, and circulating current suppression degraded. In contrast, higher ω_E values significantly improved these metrics, reducing torque and speed ripples, suppressing circulating currents, and achieving better SM capacitor voltage balancing.

2) *Thermal Performance:* Thermal performance was evaluated for varying ω_E values, as shown in Figures 5b and 6b. Higher ω_E values resulted in increased power losses and SM junction temperatures. For example, increasing ω_E from 0.1 to 0.9 caused the maximum SM junction temperature to rise from 48.74°C to 59.09°C and the maximum SM power loss to increase from 31.89 W to 43.65 W.

The results demonstrate a trade-off between thermal and electrical performance. Lower ω_E values reduced power loss and junction temperature but at the cost of increased current THD, voltage ripple, and degraded SM capacitor balancing. Conversely, higher ω_E values improved electrical performance but led to increased thermal stress. Table II summarizes the outcomes for various ω_E values, highlighting the trade-offs between electrical and thermal performance metrics.

B. *Degradation Forecasting with Deep Neural Network (DNN)*

Degradation in PEBBs significantly impacts performance, reliability, and lifespan. Due to thermal cycling, electrical stress, and environmental conditions, aging leads to increased

TABLE II
IMPACT OF WEIGHT FACTORS ON THE PERFORMANCE OF THE PROPOSED FCS-MPC METHOD

Electrical Weight Factor ω_E	Thermal Weight Factor ω_T	Phase Current Harmonics $THD_i(\%)$	Max. SM Power Loss $P_{loss}(W)$	Max. SM Junction Temperature $T_j(°C)$
0.9	0.1	5.04	43.65	59.09
0.8	0.2	8.34	42.80	58.48
0.7	0.3	9.12	41.73	57.77
0.6	0.4	9.52	40.62	56.97
0.5	0.5	9.76	39.26	55.77
0.4	0.6	11.87	38.19	54.37
0.3	0.7	14.19	37.19	53.32
0.2	0.8	18.62	34.96	50.63
0.1	0.9	26.34	31.89	48.74

power losses and reduced efficiency. Forecasting this degradation is essential for proactive maintenance and optimal control strategies. However, degradation data is scarce and obtaining accurate data is challenging due to limited availability, high costs, and confidentiality concerns. This study utilizes synthetic degradation data to analyze and incorporate aging trends into the FCS-MPC-based electro-thermal management framework. Specifically, an increase in on-state resistance is considered a key indicator of long-term degradation mechanisms, as it directly impacts power losses and thermal performance.

DNNs are used to predict power loss in PEBBs. With multiple hidden layers, DNNs effectively learn complex patterns in data, making them well-suited for degradation forecasting. The input features—current, voltage, and temperature—are preprocessed using Principal Component Analysis (PCA) to eliminate redundancy and retain essential information. The first three principal components are used as input features to ensure dimensional consistency. The DNN architecture, shown in Figure 7a, consists of three hidden layers, each with 10 neurons, utilizing the tangent sigmoid (tansig) activation function for non-linear transformations. The output layer uses a linear (purelin) activation function to predict continuous power loss values. Bayesian regularization (trainbr) is applied as the training algorithm to prevent overfitting, particularly for small datasets, through weight regularization. To improve training efficiency, the input data is normalized to address feature scaling issues. The dataset is divided into training, validation, and testing subsets to ensure thorough evaluation.

Performance metrics such as Mean Absolute Error (MAE), Mean Squared Error (MSE), and the R-squared (R^2) score are used to evaluate the network. The DNN shows great predictive accuracy, achieving a low MAE of 0.1072, an MSE of 0.0734, and an R^2 value of 0.9983 under non-degraded conditions. Under degraded conditions, it maintains high accuracy, with an MAE of 0.1208, an MSE of 0.0756, and an even higher R^2 value of 0.9996, stressing its robustness across various operational scenarios.

To quantify the impact of degradation on PEBB performance, the degradation rate cost derived from the DNN model is scaled according to how predicted power loss values exceed established thresholds, as shown in Figure 7b. These thresholds, defined by the IEEE Standard Framework for Prognostics and Health Management of Electronic Systems [14] and our prior work [11], include upper, lower, and operational failure thresholds. The degradation cost is incorporated into the FCS-MPC framework through the following objective function:

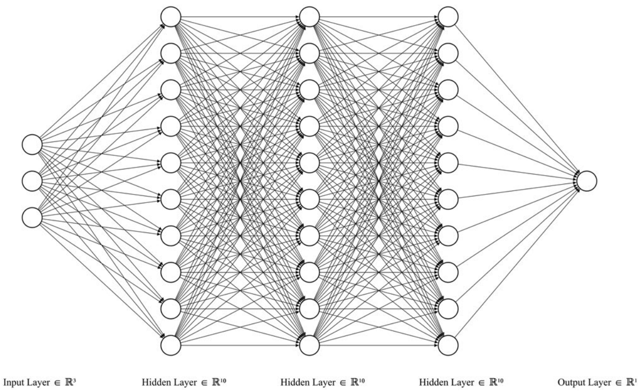

(a) DNN architecture schematic

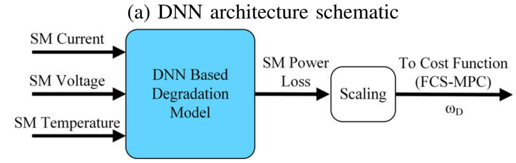

(b) DNN-based degradation model

Fig. 7. Integration of degradation model into the FCS-MPC framework

$$OF_{ETD} = \omega_E OF_E + \omega_T OF_T + \omega_D \tag{31}$$

Where ω_D represents the scaled weighting factor for the degradation rate cost. This integration enhances the FCS-MPC framework's ability to manage degradation effectively, ensuring reliable and efficient PEBB operation over time. Figure 8 presents 3D scatter plots illustrating the relationships between ω_E, ω_T, and ω_D under various operating conditions. These plots, complemented by the ranges for ω_E and ω_T detailed in Table II, provide valuable insights into their influence on system performance. The acceptable range of the degradation rate cost (ω_D), within which the electrical and thermal performance criteria remain satisfactory, is also depicted in Figure 8. Notably, this range depends on the selected value of the electrical weighting factor (ω_E). As shown, increasing ω_D reduces both the maximum SM junction temperature and the maximum SM power loss. This trend highlights the trade-offs between degradation, thermal performance, and electrical performance, allowing the proposed framework to dynamically prioritize system reliability and operational efficiency while balancing electro-thermal performance with degradation considerations.

V. CONCLUSION

This paper presents the FCS-MPC control method for the electro-thermal management of five-level PEBBs in AESs. Simulation results demonstrate the method's ability to reduce SM power losses, regulate junction temperatures, and enhance

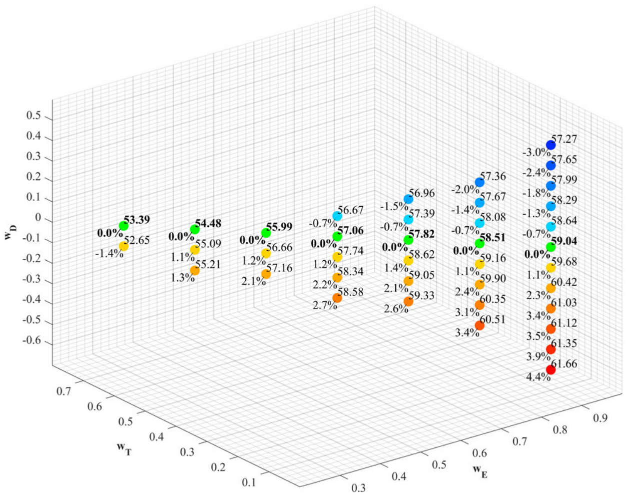

(a) Maximum SM Junction Temperature

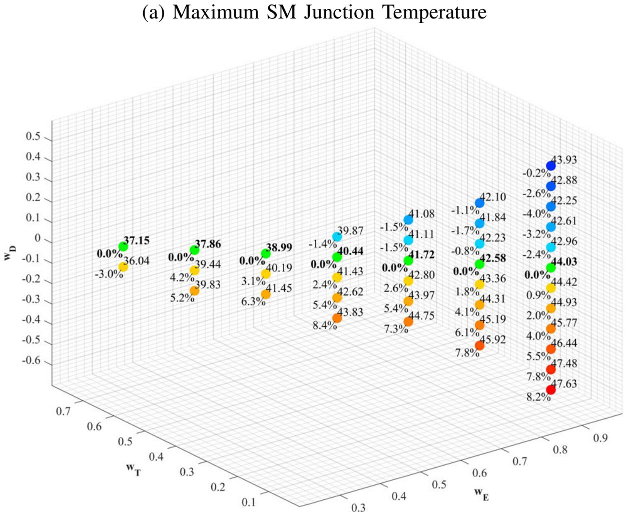

(b) Maximum SM Power Loss

Fig. 8. 3D scatter plots of w_E, w_T, and w_D

efficiency while lowering cooling system demands. These benefits are particularly advantageous for AESs with multiple PEBB stacks, improving reliability and operational performance. However, achieving these results involves trade-offs, such as increased output THD, DC-link voltage ripple, and challenges in suppressing circulating currents and balancing SM capacitor voltages. This underscores the need to balance electrical and thermal weight factors carefully.

Additionally, the integration of a DNN-based degradation model into the FCS-MPC framework enhances its long-term effectiveness. The proposed method enables proactive maintenance and optimizes PEBB performance over time by accurately predicting power loss under both non-degraded and degraded conditions. This capability ensures system reliability and efficiency while balancing electro-thermal performance and degradation considerations, contributing to more robust and resilient AES operations.

Future work will focus on the real-time implementation of the proposed electro-thermal management and degradation forecasting, further validating its effectiveness in the real world and addressing the associated trade-offs to ensure robust performance.

Acknowledgment

This material is based upon research supported by the US Office of Naval Research (ONR) under award number N00014-22-1-2558, and it is approved for public release under DCN# 2025-1-23-540. The authors would like to acknowledge the Warren H. Owen Distinguished Professorship Endowment for its support of the research effort.

References

[1] G. Sulligoi, A. Vicenzutti, and R. Menis, "All-electric ship design: From electrical propulsion to integrated electrical and electronic power systems," *IEEE Transactions on transportation electrification*, vol. 2, no. 4, pp. 507–521, 2016.

[2] T. Ericsen, N. Hingorani, and Y. Khersonsky, "Power electronics and future marine electrical systems," *IEEE transactions on industry applications*, vol. 42, no. 1, pp. 155–163, 2006.

[3] N. H. Doerry and D. H. Clayton, "Shipboard electrical power quality of service," in *IEEE Electric Ship Technologies Symposium, 2005.*, 2005, pp. 274–279.

[4] A. Moghassemi, S. I. Rahman, G. Ozkan, C. S. Edrington, Z. Zhang, and P. K. Chamarthi, "Power converters coolant: past, present, future, and a path toward active thermal control in electrified ship power systems," *IEEE Access*, 2023.

[5] A. Moghassemi, "Real-time active thermal management and degradation forecasting of power electronics building blocks in all-electric ships," Ph.D. Dissertation, Clemson University, Clemson, SC, USA, 2025.

[6] N. R. Mehrabadi, I. Cvetkovic, J. Wang, R. Burgos, and D. Boroyevich, "Busbar design for sic-based h-bridge pebb using 1.7 kv, 400 a sic mosfets operating at 100 khz," in *2016 IEEE Energy Conversion Congress and Exposition (ECCE)*, 2016, pp. 1–7.

[7] J. Falck, M. Andresen, and M. Liserre, "Active thermal control of igbt power electronic converters," in *IECON 2015-41st Annual Conference of the IEEE Industrial Electronics Society*, 2015, pp. 000 001–000 006.

[8] K. Ma, N. He, M. Liserre, and F. Blaabjerg, "Frequency-domain thermal modeling and characterization of power semiconductor devices," *IEEE Transactions on Power Electronics*, vol. 31, no. 10, pp. 7183–7193, 2015.

[9] X. Wang, Y. Wang, and A. Castellazzi, "Reduced active and passive thermal cycling degradation by dynamic active cooling of power modules," in *2015 IEEE 27th International Symposium on Power Semiconductor Devices & IC's (ISPSD)*, 2015, pp. 309–312.

[10] M. Andresen, G. Buticchi, and M. Liserre, "Study of reliability-efficiency tradeoff of active thermal control for power electronic systems," *Microelectronics Reliability*, vol. 58, pp. 119–125, 2016.

[11] A. Moghassemi, G. Ozkan, C. S. Edrington, G. Muriithi, and Z. Zhang, "Active thermal control of ac/dc power converter considering health monitoring of power modules," in *2023 IEEE Electric Ship Technologies Symposium (ESTS)*, 2023, pp. 78–85.

[12] J. Rodriguez, M. P. Kazmierkowski, J. R. Espinoza, P. Zanchetta, H. Abu-Rub, H. A. Young, and C. A. Rojas, "State of the art of finite control set model predictive control in power electronics," *IEEE Transactions on Industrial Informatics*, vol. 9, no. 2, pp. 1003–1016, 2012.

[13] U. Drofenik and J. W. Kolar, "A general scheme for calculating switching-and conduction-losses of power semiconductors in numerical circuit simulations of power electronic systems," in *Proc. IPEC*, vol. 5. Citeseer, 2005, pp. 4–8.

[14] M. Pecht, S. Mathew, L. Gullo *et al.*, "Ieee standard framework for prognostics and health management of electronic systems," *IEEE Standards Assoc., Piscataway, NJ, USA, Tech. Rep*, vol. 2017, p. 2017, 1856.